

pubs.acs.org/NanoLett Letter

Experimental and Computational Evaluation of Self-Assembled Morphologies in Diblock Janus Bottlebrush Copolymers

Runze Liu,[†] Zehao Sun,[†] Hejin Huang, Jeremiah A. Johnson,* Alfredo Alexander-Katz,* and Caroline A. Ross*



Cite This: Nano Lett. 2023, 23, 177-182



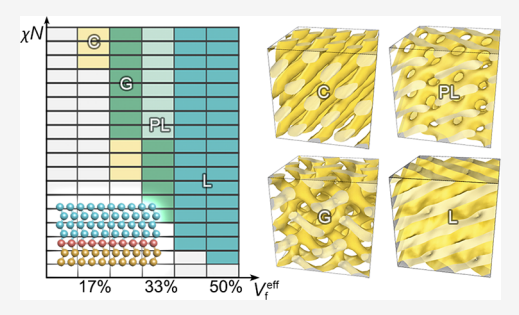
ACCESS I

III Metrics & More

Article Recommendations

s Supporting Information

ABSTRACT: Diblock Janus-type "A-branch-B" bottlebrush copolymers (di-JBBCPs) consist of a backbone with alternating A and B side chains, in contrast to the side chain arrangement of conventional bottlebrush copolymers. As a result, A and B blocks of di-JBBCPs can microphase-separate perpendicular to the backbone, which is located at the interface between the two blocks. A reparametrized dissipative particle dynamics (DPD) model is used to theoretically investigate the self-assembly of di-JBBCPs and to compare with the experimental results of a range of polystyrene-branch-polydimethylsiloxane di-JBBCPs. The experimentally formed cylinder, gyroid, and lamellar morphologies showed good correspondence with the model phase diagram, and the effect of changing volume fraction and backbone length is revealed. The DPD model predicts a bulk-stable



perforated lamella morphology together with two unconventional spherical phases, the Frank-Kasper A15 spheres and the hexagonally close-packed spheres, indicating the diversity of morphologies available from complex BCP molecular architectures.

KEYWORDS: dissipative particle dynamics, Janus bottlebrush copolymer, self-assembly, simulation, phase diagram

C elf-assembly of block copolymers (BCPs) is a scalable and efficient process for fabricating well-ordered periodic nanoscale patterns with a range of applications. ^{1–3} The tunable molecular weights⁴ and chemical compositions⁵ yield a feature size ranging from tens to several hundreds of nanometers.^{6,7} In conventional linear diblock BCPs, the periodicity of the microdomains L₀ scales with the Flory-Huggins mixing parameter χ and the degree of polymerization N as $L_0 \propto$ $\chi^{1/6}N^{2/3}$ in the strong segregation regime,⁸ and the diffusivity scales with $\exp(-\chi N)$. However, to drive microphase separation and produce sharp interfaces between microdomains, it is necessary to maintain a high value of χN during self-assembly. These competing constraints make the fabrication of well-ordered microdomains with a sub-10 nm period challenging.^{6,10} Furthermore, linear diblock copolymers (di-BCPs) produce a limited number of microdomain geometries, which do not provide all the features required for applications such as microelectronic devices.¹¹

These considerations have motivated the design of various molecular architectures such as multiblocks^{12,13} and bottle-brushes¹⁴ to increase the range of available geometries and modify the scaling behavior. Recently, an unconventional "Abranch-B" diblock Janus bottlebrush copolymer (di-JBBCP), with a pseudoalternating organization of side chains (Figure 1a) rather than the conventional blocky arrangements along the backbone, has exhibited useful properties such as reduced entanglement, improved phase separation and dense functionality.¹⁵ Moreover, the self-assembled microdomain sizes

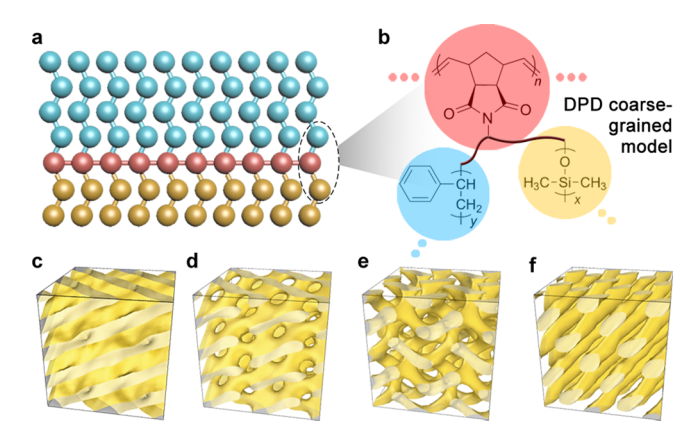


Figure 1. (a, b) A typical DPD model setup and the experimental composition of one di-JBBCP macromolecule. Each ball above represents two beads in the actual model. Beads A, B, and C corresponding to PDMS, PS, and backbone are colored yellow, blue, and red, respectively. (c–f) Snapshots of different phase structures simulated by DPD: (c) L, (d) PL, (e) G, and (f) C.

Received: October 6, 2022
Revised: December 15, 2022
Published: December 22, 2022





obtained via di-JBBCPs may be much smaller than their linear analogs. 10,16 Cheng et al. 10 demonstrated cylindrical microdomains with a 11 nm half-pitch and long-range order using a polystyrene (PS)-branch-polydimethylsiloxane (PDMS) di-JBBCP ($M_{\rm n}=609~{\rm kg~mol^{-1}})$ under solvent annealing. Guo et al. further lowered the domain size to 2.8 nm using a PS-branch-poly(lactic acid) (PLA) di-JBBCP ($M_{\rm n}=88~{\rm kg~mol^{-1}})$. In addition, the orientation of microphase separation, i.e., perpendicular to the backbone, has made it possible to form interesting hybrid X-in-Y nesting morphologies when a third block is introduced, 17 and the existence of intrinsic constraints between the neighboring blocks also promises the emergence of exciting new phases and provides diverse opportunities for nanofabrication. 18

Such molecular complexity appearing in di-, and by extension, tri-JBBCPs poses intriguing questions regarding how their phase behavior differs from that of their conventional linear BCP counterparts in the context of microdomain geometries and self-assembly dynamics. Given the formidably large parameter space to explore in the tri-JBBCP system, in this letter, we will focus our scope on the simpler di-JBBCP system. We previously demonstrated correspondences between the behavior of di- and tri-JBBCPs, giving a one-to-one mapping between the phase regions such as lamella, cylinders in di-JBBCPs and lamella-in-lamella, cylinder-in-lamella in tri-JBBCPs.¹⁸

To theoretically explore the phase structures and investigate the effect of various process parameters on BCPs, researchers have used field-based simulations, primarily self-consistent field theory (SCFT), 19-22 complex Langevin simulations, 23 and string methods, 24 to predict the final structure at equilibrium. However, field theories encounter significant cost in running time and model implementation when dealing with complex polymer architectures. 15 Furthermore, SCFT does not consider fluctuations which can affect the final structures, particularly if confinement is present, ²⁵ and fluctuating field theories have the disadvantage of being heavily controlled by discretization artifacts.²⁶ Therefore, a recent reparametrized particle-based simulation method,²⁷ dissipative particle dynamics (DPD), has been developed to model the self-assembly of diverse molecular geometries in an intuitive, straightforward way. Owing to the coarse-graining particle-based features, DPD can overcome the time- and space-scale limitations of other molecular dynamics simulations.²⁸

Here, we present the first comprehensive report using DPD to investigate the phase behaviors of a di-JBBCP, revealing order-disorder transitions, order-order transitions, and the effect of changing backbone length. The conventional phases: lamella (L), perforated lamella (PL), gyroid (G) and cylinders (C) found in di-JBBCPs are all reproduced in the phase diagram, showing good consistency with the corresponding experiments. However, strikingly different from linear di-BCPs, the perforated lamella is found to be an equilibrium bulk phase in di-JBBCPs; moreover, the sphere-forming region shows both hexagonally close-packed (HCP) spheres and the Frank-Kasper A15 spheres instead of the traditional body-centered cubic (BCC) spheres²⁹ usually captured in a linear di-BCP. Their structural features are confirmed by 3D fast Fourier transform (FFT), and they are proved to be thermodynamically stable phases by free energy profile calculations. This is the first time that these complex morphologies have been identified by DPD simulations. This work provides a basis for predicting future experimental results in other BCPs with complex architectures.

The DPD simulation was first developed to study linear di-BCPs in the pioneering work by Groot et al. 30,31 The setup for our work, however, is modified from our previously reported DPD parameters (see Methods in the Supporting Information for details). 27 Particularly, each di-JBBCP macromolecule here is represented as a 20-bead backbone grafted with 12-bead side chains as shown in the schematic in Figure 1a (each ball in the schematic represents 2 beads in the actual model). A quadratic angle potential between two adjacent bonds in the backbone is introduced to qualitatively represent the segmental stiffness, which can be tuned by the potential constant $K^{\rm A}$.

In order to validate and support our simulation, shown in Figure 1b, we also synthesize and analyze the morphologies of di-JBBCPs with the general formula $(A_x$ -branch- $B_y)_n$: A_x for PDMS with number-average molar mass (M_n) fixed at x=5.0 kg mol⁻¹, B_y for PS with varied M_n of y kg mol⁻¹, and n for the average backbone degree of polymerization (DP). The morphology is explored by varying the volume fraction (V_f) of PDMS from 0.3 to 0.5, which is achieved by choosing y=4.6, 6.9, 8.2, 9.2, and 10.3 kg mol⁻¹. For simplicity, we define these samples as Jy_n . For example, $J4.6_{30}$ has the following composition: $(PDMS_{5.0 \text{ kg mol}^{-1}}-branch$ - $PS_{4.6 \text{ kg mol}^{-1}})_{30}$.

Similar to other DPD models,³¹ the interaction between two arbitrary beads is described by a soft quadratic repulsive potential. Based on our reparametrized model,²⁷ we work with a renormalized density of 5 for which the strength between different beads is characterized by $a_{ij} \approx a_{ii} + 1.45 \chi_{ip}^{27}$ and set $a_{ii} = 15$ for the same kind of beads. This high bead density is chosen to alleviate the inherent fluctuation caused by the coarse-graining effect.³² To qualitatively represent the immiscibility in experiment, a_{AB} takes the range from 18.5 to 27.5, corresponding to $\chi_{AB}N$ in the range of 30 to 100, which is estimated by neglecting the contribution of the backbone. No interaction is set between the backbone and side chain beads. Thus, the backbone is not included in the calculation of volume fractions and free energy discussed below. Also, in order to mimic the phase separation from a disordered as-cast state to the annealed state, the simulation includes a high temperature stage with 800 000 premixing steps followed by a target temperature stage with 12 000 000 steps.

By varying the DPD repulsive interaction parameter $a_{\rm AB}$ and the effective volume fraction $V_{\rm f}^{\rm eff}$ (i.e., the volume fraction neglecting the backbone), the phase diagram at simulation density $\rho=5.0$ is constructed.²⁷ In a typical phase diagram exploration (e.g., Figure 2a), the backbone and side chain bead numbers ($N_{\rm backbone}$ and $N_{\rm side\ chain}$) are fixed to be 20 and 12 following our previous estimation¹⁸ to match the length scale of our experimental samples (see discussions in the Supporting Information), and we vary the number of PDMS and PS (labeled as A and B) side chain beads (($N_{\rm A}, N_{\rm B}$) = (2, 10), (3, 9), (4, 8), (5, 7), or (6, 6)) to quantitatively tune the effective volume fractions ($V_{\rm f}^{\rm eff}=(N_{\rm A}/(N_{\rm A}+N_{\rm B}))=17\%$, 25%, 33%, 42%, or 50%, respectively). The $V_{\rm f}^{\rm eff}$ and χN values are set with a grid interval of 8% and 4, respectively.

As shown in Figure 2a, the model exhibits a bulk-stable PL phase along with three conventional phases—L, G, and C in the nonspherical region at different $V_{\rm f}^{\rm eff}$ and χN . When the backbone is not too soft, i.e., the backbone stiffness $K^{\rm A} \geq 3.0$, these phase regions are predicted to remain unchanged regardless of the backbone stiffness (see Supplementary Figure 10 for details). The snapshots of these phases are shown in

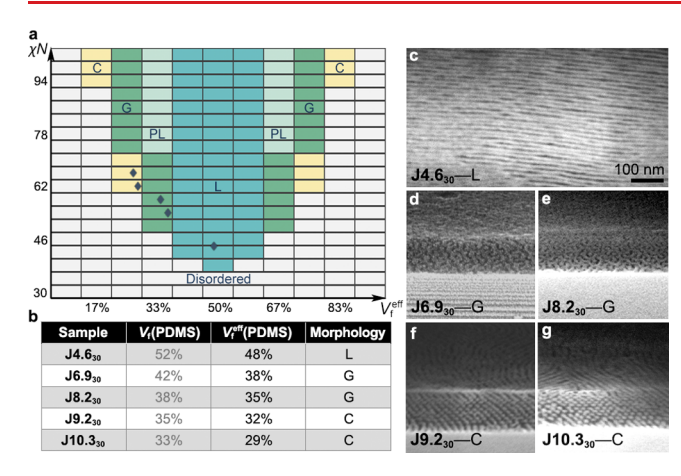


Figure 2. (a) A typical phase diagram for di-JBBCPs at $N_{\rm backbone} = 20$, $N_{\rm side~chain} = 12$, and $K^{\rm A} = 7.0$. The data points obtained experimentally are placed such that ${\bf J9.2_{30}}$ and ${\bf J10.3_{30}}$ are in the C regime and the others are scaled with N and marked accordingly. $V_{\rm f}^{\rm eff}$ represents the effective volume fraction of PDMS. (b) Property table of synthesized di-JBBCPs showing their $V_{\rm f}({\rm PDMS})$, estimated $V_{\rm f}^{\rm eff}({\rm PDMS})$ during solvent annealing, and observed morphologies in experiments. (c-g) Cross-sectional SEM images for (c) ${\bf J4.6_{30}}$, L; (d) ${\bf J6.9_{30}}$, G; (e) ${\bf J8.2_{30}}$, G; (f) ${\bf J9.2_{30}}$, C; and (g) ${\bf J10.3_{30}}$, C. All the phase structures have been reproduced.

Figure 1c–1f and Supplementary Figures 1–2 (with one representative di-JBBCP macromolecule extracted). Notably, the perforated lamellae with an ABC stacking order (Supplementary Figure 9), which is not predicted by DPD in the phase diagram of the bulk linear di-BCP system, ²⁷ is clearly shown in our di-JBBCP phase diagram. Previously, both theoretical and experimental evidence has suggested that the PL is not an equilibrium phase in linear di-BCPs, but rather a kinetically trapped structure, ^{33,34} or that a single- or double-layer PL is stabilized in the ultrathin film limit. ^{27,35,36} However, the free energy profiles shown in Supplementary Figure 3 have proved that the PL appearing here in di-JBBCPs is indeed a thermodynamically stable bulk state. A possible mechanism for the stabilization of PL is discussed later.

To check whether our DPD model can reproduce experimental results, the phase behavior of five di-JBBCP samples $J4.6_{30}$, $J6.9_{30}$, $J8.2_{30}$, $J9.2_{30}$, and $J10.3_{30}$ was characterized. For each Jy_n sample, a thin film was spin-coated followed by solvent vapor annealing in a glass chamber containing 1 mL chloroform through which a nitrogen flow of $q_{\rm N_2} = 7.0$ sccm was passed. Reactive ion etching (RIE, see Methods in the Supporting Information) is used to remove the PS block and oxidize PDMS.³⁷ The cross-sectional images of J4.6₃₀, J6.9₃₀, J8.2₃₀, J9.2₃₀, and J10.3₃₀ are observed by scanning electron microscopy (SEM) to be L, G, G, C, and C, respectively, as shown in Figure 2c-g (see Supplementary Figure 4 for top views). Since the effective volume fraction in a swelled film is correlated with the selectivity of the solvent during annealing, a quantitative model³⁸ is applied to convert $V_{\rm f}$ to $V_{\rm f}^{\rm eff}$ (see Figure 2b) based on our prior work¹⁸ when mapping to the predicted phase diagram. Hence $V_{\rm f}^{\rm eff}$ for the solvent-swelled film is the relevant comparison to the simulation parameter $V_{\rm f}^{\rm eff}$ defined in the preceding description of the simulation. The five data points are plotted on Figure 2a based on $V_{
m f}^{
m eff}$. To correlate the χN between the model and experiment, we note that the two JBBCPs with the lowest volume fractions, J10.330 and J9.230, form C and would

therefore lie within the small range of C stability predicted by the model around $\chi N=62$. Placing these points in the C region and scaling χN of the other JBBCPs according to their N, J8.2₃₀ and J6.9₃₀ lie in the G region and J4.6₃₀ in the L region. The experimental data are then all consistent with the predicted morphologies.

Di-JBBCPs are designed with a unique A-branch-B architecture, where the backbone adds an intrinsic constraint on the equilibrium configuration and the effective segregation strength between neighboring PS/PDMS blocks. We employ our DPD model to capture the effect of the segment length for backbones during microphase separation. A series of di-JBBCPs with varied $N_{\rm backbone}$ from 10 to 30 but fixed backbone stiffness ($K^{\rm A}$) and side chain lengths ($N_{\rm A}$ and $N_{\rm B}$) are generated, and their structures are studied for $V_{\rm f}^{\rm eff}$ of 25% and 33% for a range of $\chi N_{\rm c}$. As shown in Figure 3a, the phase

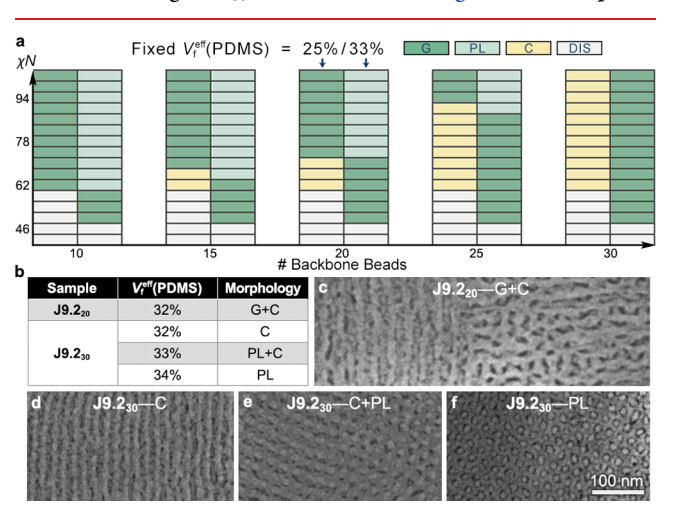


Figure 3. (a) A phase diagram for di-JBBCPs at two fixed $V_{\rm f}^{\rm eff}({\rm PDMS})$ values (25% and 33%) and $K^{\rm A}=7.0$, $N_{\rm side\ chain}=12$, but with $N_{\rm backbone}$ varying from 10 to 30. For each $N_{\rm backbone}$, the left column represents $V_{\rm f}^{\rm eff}({\rm PDMS})=25\%$ and the right column represents $V_{\rm f}^{\rm eff}({\rm PDMS})=33\%$. DIS = disordered. (b) Property table of J9.2 $_{20}$ and J9.2 $_{30}$, showing their $V_{\rm f}^{\rm eff}({\rm PDMS})$ and observed morphologies under different solvent annealing conditions. (c-f) SEM top views for (c) J9.2 $_{20}$, G mixed with C; (d) J9.2 $_{30}$ with $V_{\rm f}^{\rm eff}({\rm PDMS})=33\%$, mixed C and PL; and (f) J9.2 $_{30}$ with $V_{\rm f}^{\rm eff}({\rm PDMS})=34\%$, PL.

boundaries evolve with $N_{\rm backbone}$ at a given $V_{\rm f}^{\rm eff}$ of 25% (C/G regions) or 33% (G/PL regions), showing an expansion of the C region of stability for $V_{\rm f}^{\rm eff}$ = 25% and of the G region for $V_{\rm f}^{\rm eff}$ = 33% with increasing $N_{\rm backbone}$. These observations were quantitatively validated by the corresponding free energy profiles in Supplementary Figure 3b—h, showing that the order—order transitions at both C/G and G/PL boundaries shift to higher χN upon increasing $N_{\rm backbone}$.

As a particle-based model, DPD offers insights into the configurations of individual (macro)molecular geometries (Supplementary Figures 1 and 2). The di-JBBCP macromolecules in the simulated G structures are found to be either coiled at the 3-way nodes (Supplementary Figures 1b2 and 2b2) or stretched at the interconnecting struts (Supplementary Figures 1b3 and 2b3), which is similar to results from simulations of linear di-BCP counterparts, known as packing frustration. However, the macromolecules in the simulated C structures display only the stretched configuration (Supplementary Figures 1d2 and 2d2). Therefore, the increasing

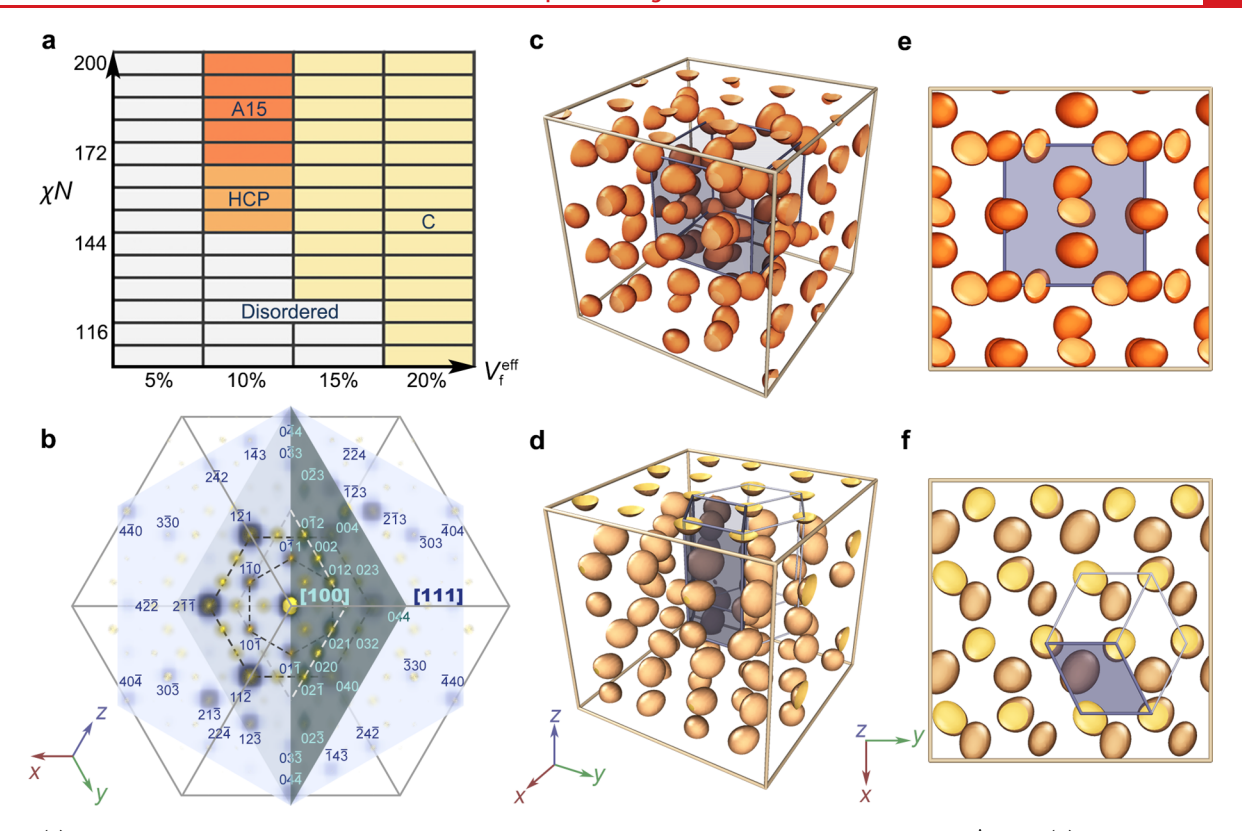


Figure 4. (a) A phase diagram for di-JBBCPs in the sphere-forming region at $N_{\text{backbone}} = 20$, $N_{\text{side chain}} = 20$, and $K^{\text{A}} = 2.0$. (b) The indexed reciprocal space patterns of the DPD-simulated A15 structure by 3D FFT, shown in an isometric view. The patterns (yellow spheres) intersected with the (100) and (111) planes (green and blue sheets, respectively) of the reciprocal lattice are approximated to the [100] and [111] ZAPs (green and blue dots), respectively (see Methods in the Supporting Information). The dashed lines connecting the points indicate the symmetry of the ZAPs. (c, d) The DPD simulated A15 and HCP structures for di-JBBCPs at $V_{\text{f}}^{\text{eff}}(\text{PDMS}) = 10\%$. (e, f) The corresponding top view of A15 and HCP structures. A unit cell is outlined in c–f.

length of backbones makes them more difficult to bend and accommodate in the G nodes, which globally stabilizes C over G at the phase boundary. Furthermore, since the spacings of interlayer PL and intralayer perforations are only determined by the side chain length, the di-JBBCPs in the simulated PL with long backbones would suffer a severely folded architecture in both inter- and intralamella positions (see Supplementary Figure 1c5-c6), which accounts for the energetic preference of the G phase at a large N_{backbone} . In the small N_{backbone} regime, on the contrary, the relieved energetic penalty in packing drives the emergence of PL as a stable phase, not observed in the linear di-BCP counterparts due to the absence of this additional degree of freedom. Since the backbones of di-JBBCPs in L (Supplementary Figures 1a2 and 2a2) and C remain extended at all backbone lengths, their regions of stability in the phase diagram hardly change with $N_{\rm backbone}$ as expected.

Experimentally, the effect of varying backbone DPs is examined by setting n=20 and 30. A clear morphology transition from a mixed G/C to pure C is shown in Figure 3c, d for J9.2₂₀ and J9.2₃₀, consistent with our predicted phase diagram. Moreover, the validation of the C/G and G/PL boundaries is examined by annealing J9.2₃₀ at different $V_{\rm f}^{\rm eff}$ as shown in Figure 3b. Technically, this is achieved by increasing the nitrogen flow rate from $q_{\rm N_2}=7$ to 14 and 30 sccm during solvent vapor annealing in the same chloroform reservoir, which effectively increases both $V_{\rm f}^{\rm eff}({\rm PDMS})$ and χN of J9.2₃₀ simultaneously. As a result, a morphology transition from C to mixed C/PL and ultimately to PL is observed in Figure 3d—

f (see cross-sectional images in Supplementary Figure 4), which follows the morphology evolution predicted by Figure 3a. It is worth noting that the obtained PL structures contain more than 10 layers and are thus not a result of ultrathin film confinement.^{27,35}

Next, the sphere-forming region in the di-JBBCP phase diagram at $V_{\rm f}^{\rm eff}$ = 10%, $N_{\rm backbone}$ = 20, $N_{\rm side\ chain}$ = 20, and $K^{\rm A}$ = 2.0 is further explored (Figure 4a). Instead of the BCC spheres dominant in linear di-BCPs, ^{13,29} two unconventional sphere arrangements, the Frank-Kasper A15 spheres (Figure 4c, e) and the HCP spheres (Figure 4d, f) are revealed in Figure 4a and demonstrated to be thermodynamically stable (see energy profiles in Supplementary Figure 5) in the high χ and low χ region, respectively. Given the complexity of these morphologies, 3D FFT is performed to further confirm the structures in reciprocal space. Previous reports tended to integrate the 3D reciprocal space signals into 1D profiles, which were then compared with scattering (e.g., SAXS) spectra. 39,40 However, a huge amount of information is lost in this integration operation, and this has typically led to rather noisy 1D profiles with only several primary peaks that could be recognized,^{39,40} likely due to the small FFT size (i.e., the simulation cell) and the existence of defects. To make full use of the 3D information, we calculate several zone-axis patterns (ZAPs) of interest and index the peaks. The ZAP characteristically reflects the selection rule of the corresponding space group, and the pattern symmetry is indicative of the symmetry of the direct lattice along the zone axis. As an exemplar, the FFT results of the simulated A15 structure in Figure 4b clearly

shows its 3-fold symmetry in the [111] ZAP and 4-fold symmetry in the [100] ZAP, and the peak indexing decisively confirms the $Pm\overline{3}n$ symmetry of the A15 structure. Other FFT results are discussed in Supplementary Figures 6–8.

The geometric configuration of one sphere-forming di-JBBCP macromolecule is displayed in Supplementary Figure 1e2 (A15) and Figure 1f2 (HCP), indicating the importance of high chemical incompatibility and low segmental stiffness in forming a severely coiled backbone sphere. Unfortunately, these conditions have not yet been achieved experimentally by tuning the chemical compositions or the solvent annealing process. It is noticed that previous explanations for the stability of HCP and A15 spheres in the linear di-BCPs were either attributed to packing frustration or extreme conformational asymmetry. However, in our di-JBBCP system, the stabilization of such unconventional sphere phases is attributed to the intrinsic confinement provided by the backbones, which leads to a delicate balance between the side chains' stretching arrangement and their intermaterial dividing surface area.

In summary, we have demonstrated a reparametrized DPD model that describes the self-assembly behaviors of a di-JBBCP. In particular, we represent each di-JBBCP molecule as a rigid backbone grafted with flexible side chains, and predict a complete phase diagram with L, PL, G, and C microstructures in good agreement with experimental observations of PDMSbranch-PS. After parametrizing the harmonic spring potential and the quadratic angle potential, the influence of the intrinsic constraint added by the backbones is revealed and validated in both simulations and experiments. Furthermore, PL here is identified both experimentally and from the model as an equilibrium bulk phase, and two unconventional spherical morphologies, the HCP spheres and the Frank-Kasper A15 spheres, are also predicted in di-JBBCP system. These three phases are uniquely stable when compared to the linear di-BCP system. Therefore, the DPD model provides a powerful tool for predicting and understanding the self-assembly behaviors applicable to various complex BCP systems.

ASSOCIATED CONTENT

Supporting Information

The Supporting Information is available free of charge at https://pubs.acs.org/doi/10.1021/acs.nanolett.2c03927.

Supplementary details including Methods sections; images for various DPD simulated morphologies with extracted backbone or macromolecule configurations; free energy profiles at phase boundaries; other top and cross-sectional SEM images; reciprocal space patterns for G, HCP, and A15; stacking details of simulated PL; influence of backbone stiffness; and tables with detailed DPD parameters (PDF)

AUTHOR INFORMATION

Corresponding Authors

Jeremiah A. Johnson – Department of Chemistry, Massachusetts Institute of Technology, Cambridge, Massachusetts 02139, United States; orcid.org/0000-0001-9157-6491; Email: jaj2109@mit.edu

Alfredo Alexander-Katz — Department of Materials Science and Engineering, Massachusetts Institute of Technology, Cambridge, Massachusetts 02139, United States; Email: aalexand@mit.edu Caroline A. Ross — Department of Materials Science and Engineering, Massachusetts Institute of Technology, Cambridge, Massachusetts 02139, United States; orcid.org/0000-0003-2262-1249; Email: caross@mit.edu

Authors

Runze Liu — Department of Materials Science and Engineering, Massachusetts Institute of Technology, Cambridge, Massachusetts 02139, United States; orcid.org/0000-0001-6040-6940

Zehao Sun — Department of Materials Science and Engineering, Massachusetts Institute of Technology, Cambridge, Massachusetts 02139, United States; orcid.org/0000-0002-9720-694X

Hejin Huang — Department of Materials Science and Engineering, Massachusetts Institute of Technology, Cambridge, Massachusetts 02139, United States;
orcid.org/0000-0002-9250-8797

Complete contact information is available at: https://pubs.acs.org/10.1021/acs.nanolett.2c03927

Author Contributions

[†]R.L. and Z.S. contributed equally to this work. The manuscript was prepared through the contribution of all authors.

Notes

The authors declare no competing financial interest.

ACKNOWLEDGMENTS

This work was supported by NSF award DMREF-2118678. The authors acknowledge the MIT Satori, the MIT Super-Cloud, MIT Research Computing Project, and Lincoln Laboratory Supercomputing Center for providing HPC resources that have contributed to the results. This work was carried out in part through the use of MIT.nano's facilities. Shared facilities of CMSE, NSL, and MRSEC under award DMR1419807 were used.

REFERENCES

- (1) Fasolka, M. J.; Mayes, A. M. Block Copolymer Thin Films: Physics and Applications. *Annu. Rev. Mater. Res.* **2001**, *31* (1), 323–355.
- (2) Hamley, I. W. Ordering in Thin Films of Block Copolymers: Fundamentals to Potential Applications. *Prog. Polym. Sci.* **2009**, 34 (11), 1161–1210.
- (3) Li, M.; Ober, C. K. Block Copolymer Patterns and Templates. *Mater. Today* **2006**, 9 (9), 30–39.
- (4) Bell, J. R.; Chang, K.; López-Barrón, C. R.; Macosko, C. W.; Morse, D. C. Annealing of Cocontinuous Polymer Blends: Effect of Block Copolymer Molecular Weight and Architecture. *Macromolecules* **2010**, *43* (11), 5024–5032.
- (5) He, X.; Liu, Y.; Zhang, R.; Wu, Q.; Chen, T.; Sun, P.; Wang, X.; Xue, G. Unique Interphase and Cross-Linked Network Controlled by Different Miscible Blocks in Nanostructured Epoxy/Block Copolymer Blends Characterized by Solid-State NMR. *J. Phys. Chem. C* **2014**, *118* (24), 13285–13299.
- (6) Bates, F. S.; Fredrickson, G. H. Block Copolymer Thermodynamics: Theory and Experiment. *Annu. Rev. Phys. Chem.* **1990**, *41* (1), 525–557.
- (7) Hashimoto, T.; Shibayama, M.; Kawai, H. Domain-Boundary Structure of Styrene-Isoprene Block Copolymer Films Cast from Solution. 4. Molecular-Weight Dependence of Lamellar Microdomains. *Macromolecules* **1980**, *13* (5), 1237–1247.

- (8) Semenov, A. N. Contribution to the Theory of Microphase Layering in Block-Copolymer Melts. *Sov. Phys. JETP* **1985**, *61* (4), 1242–1256.
- (9) Cavicchi, K. A.; Lodge, T. P. Self-Diffusion and Tracer Diffusion in Sphere-Forming Block Copolymers. *Macromolecules* **2003**, *36* (19), 7158–7164.
- (10) Cheng, L.-C.; Gadelrab, K. R.; Kawamoto, K.; Yager, K. G.; Johnson, J. A.; Alexander-Katz, A.; Ross, C. A. Templated Self-Assembly of a PS- *Branch* -PDMS Bottlebrush Copolymer. *Nano Lett.* **2018**, *18* (7), 4360–4369.
- (11) Ross, C. A.; Berggren, K. K.; Cheng, J. Y.; Jung, Y. S.; Chang, J.-B. Three-Dimensional Nanofabrication by Block Copolymer Self-Assembly. *Adv. Mater.* **2014**, *26* (25), 4386–4396.
- (12) Eagan, J. M.; Xu, J.; Di Girolamo, R.; Thurber, C. M.; Macosko, C. W.; LaPointe, A. M.; Bates, F. S.; Coates, G. W. Combining Polyethylene and Polypropylene: Enhanced Performance with PE/ *i* PP Multiblock Polymers. *Science* **2017**, 355 (6327), 814–816.
- (13) Bates, C. M.; Bates, F. S. 50th Anniversary Perspective: Block Polymers—Pure Potential. Macromolecules 2017, 50 (1), 3-22.
- (14) Rempp, P.; Lutz, P.; Masson, P.; Chaumont, P. Macromonomers: A New Class of Polymeric Intermediates in Macromolecular Synthesis II Homo- and Copolymerization. *Makromol. Chem.* **1985**, *13* (S19851), 47–66.
- (15) Kawamoto, K.; Zhong, M.; Gadelrab, K. R.; Cheng, L.-C.; Ross, C. A.; Alexander-Katz, A.; Johnson, J. A. Graft-through Synthesis and Assembly of Janus Bottlebrush Polymers from A-Branch-B Diblock Macromonomers. J. Am. Chem. Soc. 2016, 138 (36), 11501–11504.
- (16) Guo, Z.; Le, A. N.; Feng, X.; Choo, Y.; Liu, B.; Wang, D.; Wan, Z.; Gu, Y.; Zhao, J.; Li, V.; Osuji, C. O.; Johnson, J. A.; Zhong, M. Janus Graft Block Copolymers: Design of a Polymer Architecture for Independently Tuned Nanostructures and Polymer Properties. *Angew. Chem., Int. Ed.* **2018**, *57* (28), 8493–8497.
- (17) Liang, R.; Xue, Y.; Fu, X.; Le, A. N.; Song, Q.; Qiang, Y.; Xie, Q.; Dong, R.; Sun, Z.; Osuji, C. O.; Johnson, J. A.; Li, W.; Zhong, M. Hierarchically Engineered Nanostructures from Compositionally Anisotropic Molecular Building Blocks. *Nat. Mater.* **2022**, *21* (12), 1434–1440.
- (18) Sun, Z.; Liu, R.; Su, T.; Huang, H.; Kawamoto, K.; Liang, R.; Liu, B.; Zhong, M.; Alexander-Katz, A.; Ross, C. A.; Johnson, J. A. Emergence of Layered Nanoscale Mesh Networks through Intrinsic Molecular Confinement Self-Assembly. *Nat. Nanotechnol.* **2022** accepted, DOI: 10.1038/s41565-022-01293-z.
- (19) Sides, S. W.; Fredrickson, G. H. Continuous Polydispersity in a Self-Consistent Field Theory for Diblock Copolymers. *J. Chem. Phys.* **2004**, *121* (10), 4974–4986.
- (20) Sides, S. W.; Fredrickson, G. H. Parallel Algorithm for Numerical Self-Consistent Field Theory Simulations of Block Copolymer Structure. *Polymer* **2003**, *44* (19), 5859–5866.
- (21) Ceniceros, H. D.; Fredrickson, G. H. Numerical Solution of Polymer Self-Consistent Field Theory. *Multiscale Model. Simul.* **2004**, 2 (3), 452–474.
- (22) Hannon, A. F.; Ding, Y.; Bai, W.; Ross, C. A.; Alexander-Katz, A. Optimizing Topographical Templates for Directed Self-Assembly of Block Copolymers via Inverse Design Simulations. *Nano Lett.* **2014**, *14* (1), 318–325.
- (23) Villet, M. C.; Fredrickson, G. H. Efficient Field-Theoretic Simulation of Polymer Solutions. *J. Chem. Phys.* **2014**, *141* (22), 224115.
- (24) E, W.; Ren, W.; Vanden-Eijnden, E. String Method for the Study of Rare Events. *Phys. Rev. B* **2002**, *66* (5), 052301.
- (25) Alexander-Katz, A.; Fredrickson, G. H. Diblock Copolymer Thin Films: A Field-Theoretic Simulation Study. *Macromolecules* **2007**, *40* (11), 4075–4087.
- (26) Alexander-Katz, A.; Moreira, A. G.; Sides, S. W.; Fredrickson, G. H. Field-Theoretic Simulations of Polymer Solutions: Finite-Size and Discretization Effects. *J. Chem. Phys.* **2005**, *122* (1), 014904.
- (27) Huang, H.; Alexander-Katz, A. Dissipative Particle Dynamics for Directed Self-Assembly of Block Copolymers. *J. Chem. Phys.* **2019**, *151* (15), 154905.

- (28) Hoogerbrugge, P. J.; Koelman, J. M. V. A. Simulating Microscopic Hydrodynamic Phenomena with Dissipative Particle Dynamics. *Europhys. Lett. EPL* **1992**, *19* (3), 155–160.
- (29) Bates, F. S.; Hillmyer, M. A.; Lodge, T. P.; Bates, C. M.; Delaney, K. T.; Fredrickson, G. H. Multiblock Polymers: Panacea or Pandora's Box? *Science* **2012**, 336 (6080), 434–440.
- (30) Groot, R. D.; Warren, P. B. Dissipative Particle Dynamics: Bridging the Gap between Atomistic and Mesoscopic Simulation. *J. Chem. Phys.* **1997**, *107* (11), 4423–4435.
- (31) Groot, R. D.; Madden, T. J. Dynamic Simulation of Diblock Copolymer Microphase Separation. *J. Chem. Phys.* **1998**, *108* (20), 8713–8724.
- (32) Huang, H. Designing and Fabricating 3D Nanostructures through Directed Self-Assembly of Block Copolymers. *Doctoral Thesis*; Massachusetts Institute of Technology, Cambridge, MA, 2021. https://dspace.mit.edu/handle/1721.1/139939 (accessed 2022-06-23).
- (33) Qi, S.; Wang, Z.-G. Kinetics of Phase Transitions in Weakly Segregated Block Copolymers: Pseudostable and Transient States. *Phys. Rev. E* **1997**, *55* (2), 1682–1697.
- (34) Hajduk, D. A.; Takenouchi, H.; Hillmyer, M. A.; Bates, F. S.; Vigild, M. E.; Almdal, K. Stability of the Perforated Layer (PL) Phase in Diblock Copolymer Melts. *Macromolecules* **1997**, *30* (13), 3788–3795
- (35) Bai, W.; Hannon, A. F.; Gotrik, K. W.; Choi, H. K.; Aissou, K.; Liontos, G.; Ntetsikas, K.; Alexander-Katz, A.; Avgeropoulos, A.; Ross, C. A. Thin Film Morphologies of Bulk-Gyroid Polystyrene-Block-Polydimethylsiloxane under Solvent Vapor Annealing. *Macromolecules* **2014**, 47 (17), 6000–6008.
- (36) Lee, S.; Cheng, L.-C.; Gadelrab, K. R.; Ntetsikas, K.; Moschovas, D.; Yager, K. G.; Avgeropoulos, A.; Alexander-Katz, A.; Ross, C. A. Double-Layer Morphologies from a Silicon-Containing ABA Triblock Copolymer. *ACS Nano* **2018**, *12* (6), 6193–6202.
- (37) Jung, Y. S.; Ross, C. A. Orientation-Controlled Self-Assembled Nanolithography Using a Polystyrene-Polydimethylsiloxane Block Copolymer. *Nano Lett.* **2007**, *7* (7), 2046–2050.
- (38) Hannon, A. F.; Bai, W.; Alexander-Katz, A.; Ross, C. A. Simulation Methods for Solvent Vapor Annealing of Block Copolymer Thin Films. *Soft Matter* **2015**, *11* (19), 3794–3805.
- (39) Martínez-Veracoechea, F. J.; Escobedo, F. A. Simulation of the Gyroid Phase in Off-Lattice Models of Pure Diblock Copolymer Melts. J. Chem. Phys. **2006**, 125 (10), 104907.
- (40) Padmanabhan, P.; Martinez-Veracoechea, F. J.; Araque, J. C.; Escobedo, F. A. A Theoretical and Simulation Study of the Self-Assembly of a Binary Blend of Diblock Copolymers. *J. Chem. Phys.* **2012**, *136* (23), 234905.
- (41) Zhang, C.; Vigil, D. L.; Sun, D.; Bates, M. W.; Loman, T.; Murphy, E. A.; Barbon, S. M.; Song, J.-A.; Yu, B.; Fredrickson, G. H.; Whittaker, A. K.; Hawker, C. J.; Bates, C. M. Emergence of Hexagonally Close-Packed Spheres in Linear Block Copolymer Melts. J. Am. Chem. Soc. 2021, 143 (35), 14106–14114.
- (42) Bates, M. W.; Lequieu, J.; Barbon, S. M.; Lewis, R. M.; Delaney, K. T.; Anastasaki, A.; Hawker, C. J.; Fredrickson, G. H.; Bates, C. M. Stability of the A15 Phase in Diblock Copolymer Melts. *Proc. Natl. Acad. Sci. U. S. A.* **2019**, *116* (27), 13194–13199.